

Fan Broadband Interaction Noise Modeling

Sheryl Grace ^{*} and Andy Wixom [†] and Julian Winkler [‡] and Douglas Sondak [§]

Boston University, Boston, MA 02215

and Michaela M. Logue [¶]

University of Notre Dame, Notre Dame, IN 46656

Results from a detailed investigation into the effect of modeling assumptions used with the RSI method to compute broadband interaction noise downstream of a turbofan engine's fan stage are presented. The modeling assumptions that are considered include the use of a Green's function to obtain the exhaust noise from the unsteady vane surface pressure, the implementation of a 2D vs. 3D vane model, and the form of the turbulence velocity correlation function. Calculation of the duct acoustics via the Green's function is shown to be robust when one selects the frequencies used for the calculation such that they do not coincide with a duct cut-on/cut-off edge frequency. The unsteady vane response calculated by strip theory is found to be different than that predicted with a three-dimensional vane model. However, it is not clear yet how these differences specifically impact the predicted exhaust noise. Inclusion of the inhomogeneity of the turbulence across the passage is not so important because the average passage value provides good results. The form of the correlation function used to model the inflow turbulence is shown to have a strong impact on the overall sound power level. Within the RSI framework, it is shown that using a common 3D spectrum (e. g. Liepmann and Gaussian spectra) but disregarding the k_3 contribution gives results 20 dB lower than when the nontraditional RSI spectrum is used. The inclusion of the k_3 effect with the common 3D spectrum within RSI leads to a difference of 10 dB instead of 20 dB; however, the physical argument for including k_3 effects on each 2D vane strip is unknown.

I. Introduction

The acoustic prediction of broadband turbofan, fan-stage, interaction noise is considered. The RSI code for broadband noise prediction serves as a platform for the investigation of the impact of various modeling assumptions on the accuracy of such a prediction. Results from the RSI prediction are compared to predictions from BB3D a 3-D broadband response code.¹

Predictions from the RSI method for the scaled turbofan used in the source diagnostic test (SDT) have been reported previously.²⁻⁴ The sensitivity of the original RSI predictions to modeling choices such as stagger angle and background turbulence intensity has already been investigated.⁵ In this paper, the sensitivity study is continued and expanded. The topics that are addressed include

1. Effect of using the Green's function method to obtain acoustic power in the duct.
2. Effect of the strip theory assumption on the prediction of vane unsteady loading.

^{*}Assoc. Prof., Dept. Mech. Eng., Associate Fellow, AIAA. sgrace@bu.edu.

[†]Graduate student, Dept. of Mech. Eng., student member AIAA.

[‡]Research Associate, Dept. of Mech. Eng., student member AIAA.

[§]Scientific Computing and Visualization, Member AIAA.

[¶]Research associate, Dept. of Aero. and Mech. Eng.

3. Effect of including spanwise wave number variation on each cascade strip.
4. Effect of modeling the inhomogeneity of the turbulent kinetic energy across a passage.
5. Effect of varying the form of the turbulence correlation function on the final prediction.
6. Effect of the 2D flat-plate, strip-theory, vane model as compared to the 3D cambered vane model.

The SDT geometry and flow cases are used to carry out the study. Sec. II describes the RSI and BB3D methods. The outcomes from studying the six effects listed above are described in Sec. IV. Conclusions based on these studies and planned future investigations are then described in Sec. V.

II. Method

Both of the methods described in this paper are derived based on the Linearized Euler Equations valid for inviscid, subsonic mean flows. The flow perturbations and unsteady surface response are assumed to be small. The RSI method models the fan exit guide vanes (FEGVs) as strips from hub-to-tip of infinite flat cascades in which the inflow is 2D and aligned perfectly with the cascade vanes. Therefore, the mean flow quantities are constant and inflow swirl is neglected. The vane geometry at a each spanwise strip is matched to the actual geometry by selecting the appropriate chordlength and the stagger angle. The selection of the stagger angle has been shown to significantly affect the results and it is investigated again in this paper. The simplifying assumptions allow a single integral equation to be solved in order to determine the unsteady pressure distribution on a cascade section due to a vortical flow disturbance (i.e., gust). The derivation of the integral equation and its solution as used by RSI are attributed to Ventres.⁶ Previously, the unsteady response on a cascade strip found using the Ventres method has been compared to that found using the two-dimensional rectilinear cascade method. The comparisons show exact agreement.⁷ The simplifying assumptions result in a very efficient calculation process in which an entire spectrum can be predicted in less than an hour. The trade-off in accuracy for efficiency is explored in this paper

The BB3D method also utilizes velocity splitting within the Linearized Euler Equations. It then solves the resulting system of equations numerically. The FEGVs are modeled as three-dimensional and the computational domain is taken as one blade passage. The mean inflow includes swirl and the formulation allows for spatial variation of the mean flow in all directions. The grid and geometry are determined through an iterative process in which the mean flow Mach number and angle in the duct upstream and downstream of the vane is matched. Once the mean flow is matched, the pressure side of the vane geometry is placed on the upper most streamline and the suction side of the vane geometry is placed on the lower most streamline with an axial position that reflects the original geometry. Thus the vanes are cambered and twisted but may not actually be true airfoils with closed leading and trailing edges if the suction and pressure sides were put together. The mean flow gradients distort the fully 3D gust in this method and as such different results are expected as compared to the 2D flat-plate results. Once the mean flow iteration is complete and the vane geometry is set, the response to a single gust is computed using BB3D in about 20 minutes. Broadband calculations that require the vane response at multiple modes and frequencies can take up to 2 weeks to complete on a single processor. The impact of the more realistic geometry and flow model on the vane response and associated duct acoustics in light of the required computational time is considered here.

A. The Green's function method

In the 2D method, the response of each spanwise strip to unit amplitude upwash disturbances at all modes of interest is computed. The influence of the full vane response on the duct acoustics is then computed using the Green's function for an infinite annulus. Therefore geometry variations in the duct downstream of the vane are neglected. The Green's function for the annulus is nominally given as

$$G(\vec{y}, \tau | \vec{x}, t) = \frac{i}{4\pi} \sum_{m=-\infty}^{m=\infty} \sum_{n=-\infty}^{n=\infty} \frac{\Psi_{m,n}(y_2, y_3) \Psi_{m,n}^*(x_2, x_3)}{k_{m,n} \Gamma_{m,n}} \exp \left\{ i \left[\omega(\tau - t) + \frac{Mk_0}{\beta^2} (y_1 - x_1) + \frac{k_{m,n}}{\beta^2} |y_1 - x_1| \right] \right\} \quad (1)$$

where \vec{x} and \vec{y} represent two locations in the annulus respectively with x_1 being the axial coordinate, $k_0 = \omega/c_\infty$ with c_∞ and M being the mean speed of sound and Mach number in the annulus, and

$$k_{m,n} = \sqrt{k_0 - \kappa_{m,n}} \quad (2)$$

where $\kappa_{m,n}$ and $\Psi_{m,n}$ are the eigenvalues and eigenfunctions for the annulus. Full description of the Green's function has been described previously.^{8,9} The relationship between the frequency, ω , and the eigenvalues, $\kappa_{m,n}$, dictate which modes are cut on in the annulus.

The 3D formulation in BB3D consists of a numerical solution in a domain defined by the duct geometry. The acoustic pressure on the duct inlet and exit boundary are written such that the modal amplitudes on the boundary are solved simultaneously with the entire pressure field.

B. Turbulence spectrum

The turbulence spectrum must be selected as part of the model. If one follows the derivation in Hinze¹⁰ and Pope¹¹ the spectrum for isotropic turbulence can be generated based on the Fourier transform of the streamwise velocity correlation of any velocity component. Some background regarding possible forms of the spectrum is provided here.

First, basic definitions for the average value and the transform pair are needed

$$\langle u_1(t)u_1(t+\tau) \rangle = \lim_{T \rightarrow \infty} \frac{1}{2T} \int_{-T}^T u_1(t)u_1(t+\tau)dt \quad (3)$$

$$\langle u_1(t)u_1(t+\tau) \rangle = \int_{-\infty}^{\infty} \phi_1(f)e^{i2\pi f\tau}df \quad (4)$$

$$\phi_1(f) = \int_{-\infty}^{\infty} \langle u_1(t)u_1(t+\tau) \rangle e^{-i2\pi f\tau}d\tau \quad (5)$$

When the Taylor's hypothesis holds and the turbulence is convected by the mean flow then $k_1 = 2\pi f/\langle U \rangle$ where $\langle U \rangle$ is the mean flow average value. Therefore, the related one dimensional spectrum can be written in either the frequency or wave-number domain via

$$\phi_1(k_1) = \frac{\phi_1(f)\langle U \rangle}{2\pi}. \quad (6)$$

The basic correlation is defined as

$$R_{ij}(\vec{r}, t) = \langle u_i(\vec{x}, t)u_j(\vec{x} - \vec{r}, t) \rangle \quad (7)$$

and the velocity spectrum tensor transform pair becomes

$$\Phi_{ij}(\vec{k}, t) = \frac{1}{(2\pi)^3} \int \int \int R_{ij}(\vec{x}, t)e^{-i\vec{k}\cdot\vec{x}}d\vec{x} \quad (8)$$

$$R_{ij}(\vec{x}, t) = \int \int \int \Phi_{ij}(\vec{k}, t)e^{i\vec{k}\cdot\vec{x}}d\vec{k} \quad (9)$$

If Eq. (9) is integrated using spherical coordinates and a focus placed on the $i - i$ th component of the tensor then

$$R_{ii}(r, t) = \int_0^\infty \int_0^{2\pi} \int_0^\pi \Phi_{ii}(k, t)k^2 \sin\theta e^{ikr \cos\theta} d\theta d\phi dk \quad (10)$$

$$\Phi_{ii}(k, t) = \frac{1}{(2\pi)^3} \int_0^\infty \int_0^{2\pi} \int_0^\pi R_{ii}(r, t)r^2 \sin\theta e^{-ikr \cos\theta} d\theta d\phi dk \quad (11)$$

where $k^2 = k_1^2 + k_2^2 + k_3^2$ and $r^2 = x_1^2 + x_2^2 + x_3^2$.

In both Pope¹¹ and Hinze,¹⁰ the general form of the spectrum tensor for isotropic turbulence is given as

$$\Phi_{ij}(\vec{k}, t) = -\frac{E(k, t)}{4\pi k^2} \left(\frac{k_i k_j}{k^2} - \delta_{ij} \right) \quad (12)$$

The intermediate function, E can be seen as a generating function such that

$$E_{11}(k_1) = \int_{k_1}^{\infty} \frac{E(k)}{k} \left(1 - \frac{k_1^2}{k} \right) dk \quad (13)$$

is the transform of the longitudinal spatial correlation function, f , normalized by the turbulence intensity u_1^2 . For isotropic turbulence, the lateral correlation function, g , is related to f via

$$g(x) = f(x) + \frac{x}{2} \frac{\partial f(x)}{\partial x} \quad (14)$$

The length scales in the longitudinal and lateral directions are defined in terms of f and g respectively as

$$\Lambda_1 = \int_0^{\infty} f(x) dx \quad (15)$$

$$\Lambda_1 = \int_0^{\infty} g(x) dx \quad (16)$$

The most commonly used 3D spectrum are the Liepmann, Gaussian and von Karman models. It has been shown previously, that the Liepmann and von Karman models are very similar¹² and as such this paper will only consider Liepmann and Gaussian spectra. The 1D spatial correlation functions that give rise to Liepmann and Gaussian spectra are

$$f_L(x_1) = e^{-x_1/\Lambda_1} \quad (17)$$

$$f_G(x_1) = e^{-(x_1/\Lambda_1)^2} \quad (18)$$

whose Fourier Transforms multiplied by the turbulence intensity are

$$E_{11,L}(k_1) = \frac{2}{\pi} u_1^2 \frac{\Lambda_L}{1 + (k_1 \Lambda_L)^2} \quad (19)$$

$$E_{11,G}(k_1) = \frac{2}{\pi^2} u_1^2 \Lambda_L e^{-(k_1 \Lambda_L)^2/\pi} \quad (20)$$

$$(21)$$

The related intermediate spectral functions are

$$E_L(k) = \frac{8u_1^2 \Lambda_L}{\pi^2} \frac{(k \Lambda_L)^4}{(1 + (k \Lambda_L)^2)^3} \quad (22)$$

$$E_G(k) = \frac{4u_1^2 \Lambda_L}{\pi^3} (k \Lambda_L)^4 e^{-(k \Lambda_L)^2/\pi} \quad (23)$$

III. Experimental results used for comparison

The results in this paper were all generated for cases taken from the Source Diagnostic Test (SDT). The SDT utilized a 22 inch NASA/GE 1/5 scaled fan rig with 22 rotor blades and interchangeable FEGVs. Both the baseline and low-count cases are discussed here. The baseline case consisted of 54 unswept vanes while the low-count had 26 unswept vanes. The fan chord is 3.61 inches and the vane chord for the baseline and low count cases are 1.57 and 3.26 inches respectively at the pitchline. Wake measurements were made at

two positions: mid-gap and just upstream of the vane leading edge (the measurements were made when the swept vane assembly was installed). LDV data were obtained at several speeds, three of which are considered in this study: approach (7,808 rpm), cut-back (11,075 rpm), and take-off (12,657 rpm).¹³ Hot-wire data were obtained at 6,329 rpm (off-design) and 7,808 rpm only. Finally, field microphone measurements were taken in order to quantify the exhaust duct broadband sound power levels.¹⁴

IV. Results

A. Effect of using the Green’s method to obtain acoustic power in the duct

The RSI method builds the unsteady pressure jump on a vane from hub-to-tip using a strip theory approach and then utilizes the Green’s function method to obtain the acoustic power in the duct. As is shown in Eq. (1), the transfer function is singular when $k_{m,n}$ is zero. This occurs at the edge frequencies between cut-off and cut-on duct modes. In the RSI method, the duct is approximated to be of include semi-infinite extent and constant annular cross-section. Therefore, the duct eigenvalues $\kappa_{m,n}$ can be obtained *a priori*; and, the edge frequencies can also be identified *a priori*. Figure A shows the results when singular and nonsingular frequencies are used in the RSI method.

It is clear that if edge frequencies are selected, especially at the lower frequencies, incorrect results are obtained. Throughout this paper, only non-singular frequencies are used to obtain the broadband predictions.

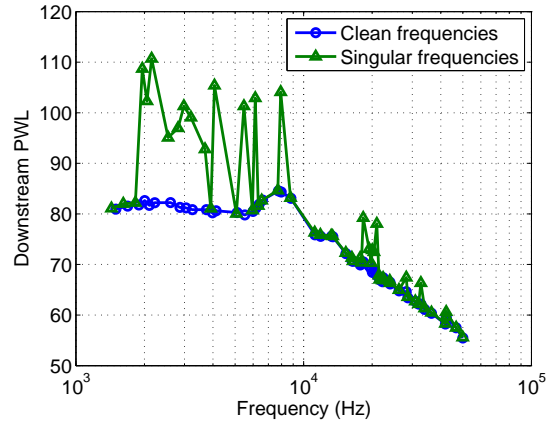


Figure 1. RSI predictions when singular and nonsingular frequencies are used (based on duct mode cut-on). Baseline vane case at approach. Leading edge stagger. Liepmann Spectrum.

B. Effect of the strip theory assumption on the prediction of vane unsteady loading

One draw back of the 2D method utilized in RSI is the occurrence of cascade resonance at various span locations. Cascade resonance is a function of the stagger and vane-to-vane spacing and thus the associated interblade phase angle. The mosaic of plots in Figure 2 shows the spanwise lift distribution obtained using strip theory by mode at several frequencies for the SDT baseline vane at approach case. In these simulations, only $k_3 = 0$ was used at each strip.

At lower frequencies, below about 5,500 Hz, the 0th mode does not dominate whereas beyond this frequency for the most part it does dominate. Starting at about 5500 Hz, the effect of cascade resonance can be seen. The resonance moves from strip to strip as the frequency changes. This is better viewed by simply plotting the 0th mode at various frequencies as in Figure 3. The strong resonance that occurs at 5500 Hz resides near 70% span and this seems to affect the exhaust sound power level prediction as will be seen in Figure 6. When the resonance occurs between 0 and 50% span, the influence on the final sound prediction is not as strong. It was shown by Logue et al.¹⁵ that the resonance is particular to the linear cascade and it does not occur when three-dimensional vanes are modeled. This will also be demonstrated later.

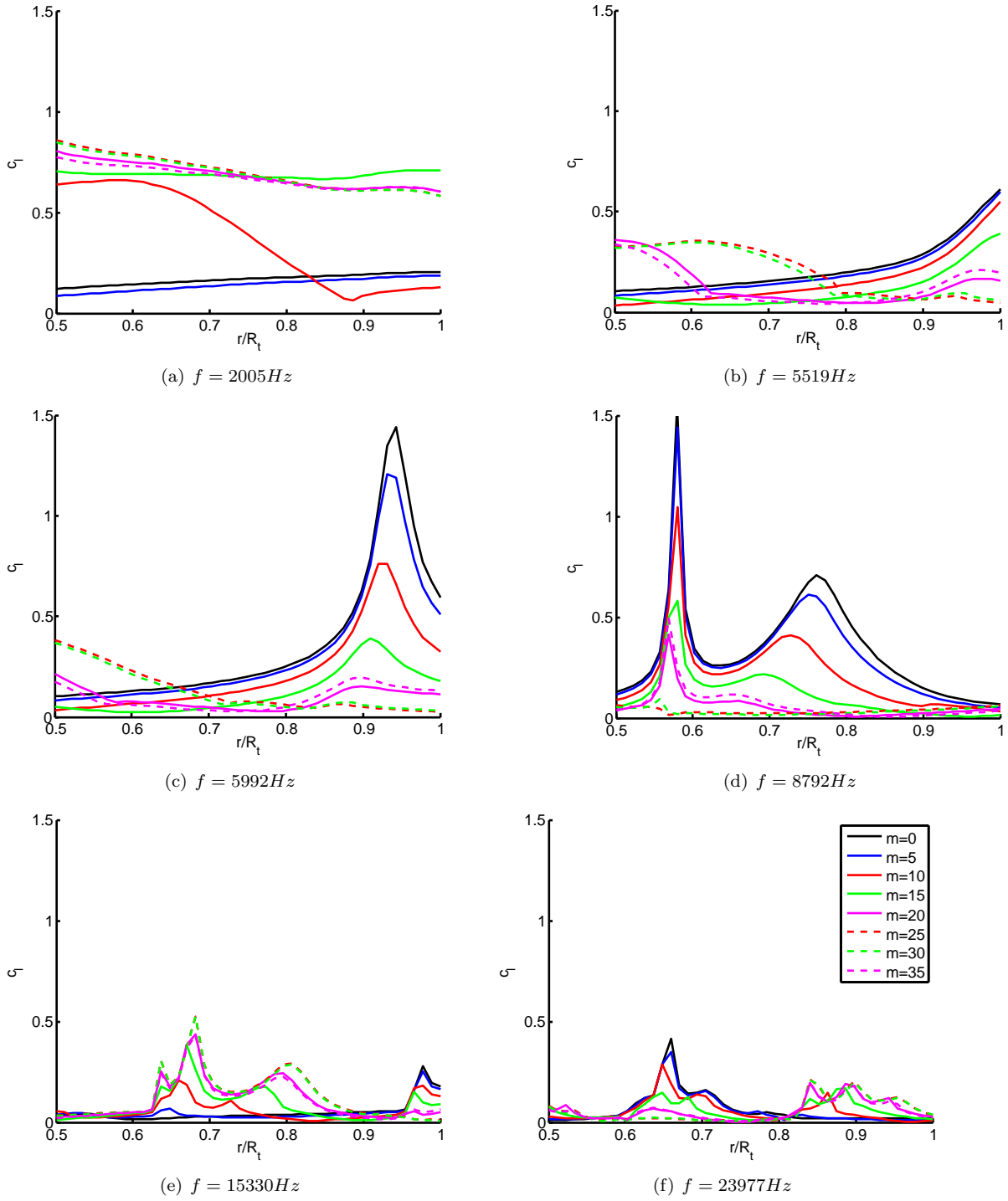


Figure 2. Lift on spanwise strips as a function of mode number. SDT baseline case at approach. Trailing edge stagger.

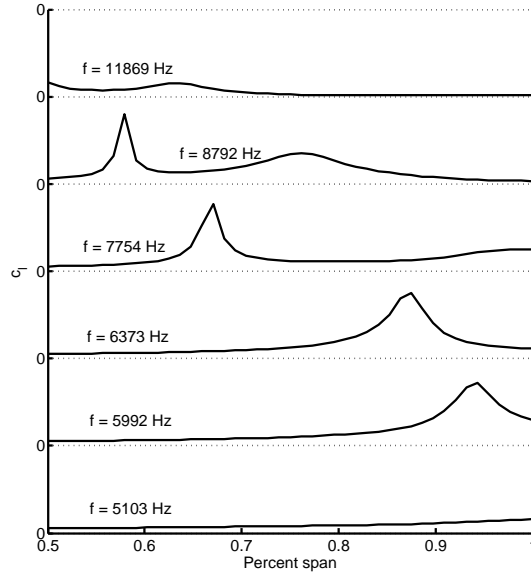


Figure 3. Lift on spanwise strips from hub to tip for 0th mode number at various frequencies. Baseline vane case at approach. Trailing edge stagger.

C. Effect of including spanwise wave number variation on each cascade strip.

The original RSI formulation did not include spanwise wave number effects. The formulation leads to an end result shown in Eq. (48) where the turbulence spectrum is initially expressed as $R(x_1, x_2)R_r(r)$ and then its transform takes a form $\Phi(k_1, k_2)R_r(r)$. The 3D correlation function $R(x_1, x_2, x_3)$ transforms to $\Phi(k_1, k_2, k_3)$.

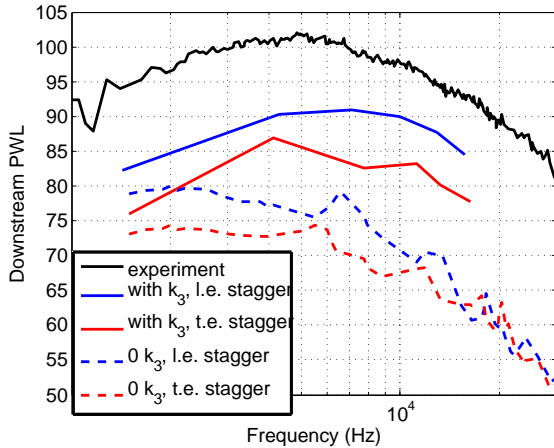


Figure 4. Exhaust PWL predicted using only 0th spanwise wave number and all cut-on spanwise wavenumber on each strip. Baseline vane case at approach. Stagger as labeled. Turbulence background level only. Liepmann spectrum.

The rationale behind the original assumption on the form of the correlation function was based on the following argument. The isotropic turbulence assumption that is used in the formulation dictates that the spanwise correlation length is less than the streamwise correlation length. For the SDT geometry and wake flow, this translates into spanwise correlation lengths on the order of 2% of the span. Therefore it was deduced that if the spanwise strips are selected to be slightly larger than the length scale, there is no need to include lower values of the spanwise wave number because they would not satisfy the spanwise strip boundary conditions. Furthermore, higher spanwise wave numbers should lead to sub-critical response of the cascade which would only minimally impact the predicted sound from the the Green's function method.

Other methods do include the effect of a spanwise wave number.^{12,16,17} As such, a preliminary test was

run to include a spanwise wave number effect in the current RSI calculation. On each strip a general Fourier transform is allowed so that the term $e^{ik_3 r}$ now appears. At this time, only supercritical vane response is included in the formulation. A k_3 increment of 0.0625 is sufficient to converge the numerical integration and is used to obtain the results in Figure 4. Only the background turbulence level was used in this test calculation.

The results were obtained by using only the background turbulence level as input which will be discussed at more length in the next section. (i.e. the black dashed line is identical to the light blue line in Fig. 6.) The inclusion of the supercritical k_3 on each strip increases the overall spectrum about 10 dB for this case. The results actually compare much better with the experimental values and with the predictions reported by Posson for the same case using a very similar method.¹⁶ Indeed, as will be shown in the next section, had the average passage value of the turbulence intensity been used instead of the background value, the results would be 3-5 dB higher and in even better agreement.

The physical meaning of including the k_3 effect on each strip however is still unclear as described above. More effort must be given to understanding what physical mechanism is included when k_3 is utilized and if it is compatible with the strip-theory assumption and the requirement for very small correlation lengths in the spanwise direction.

D. Effect of modeling the inhomogeneity of the turbulent kinetic energy across a passage.

The RSI methodology models the inhomogeneity of the wake turbulence as a Gaussian distribution set on top of a background turbulence level. This is shown in Figure 5. In the RSI derivation, treatment of the background and wake-like portions of the turbulent kinetic energy across the passage leads to 3 contributions to the expected value of the turbulent inflow wavenumber-frequency spectrum.

The three terms correspond to the background turbulence only, the wake turbulence only, and the background/wake turbulence cross term. (Posson¹⁶ neglects the 3rd term based on physical arguments.) Other broadband simulation methods do not include the inhomogeneity explicitly.^{12,17} Instead they use an average value of the TKE on the passage. The effect of including the inhomogeneity was tested and the results are shown in Figure 6. The results from four simulations performed with RSI are shown: 1) the background TKE level is used and the wake terms are neglected, 2) the average passage value of TKE is used as the background value and the wake terms are neglected, 3) all three terms are used to describe the TKE distribution, 4) the maximum TKE value on the passage is used as the background value and the wake terms are neglected. Good agreement at frequencies less than 15 kHz is seen between the results when all three terms are used to describe the TKE and when the average passage value of the TKE is used. Inclusion of the inhomogeneity affects the higher frequencies more as the prediction becomes closer to the prediction using the maximum TKE level rather than the prediction using the average passage value. This phenomenon is not yet fully understood. However, the relatively good agreement with the average passage based results indicates that using the average passage in RSI to accomplish comparisons with other codes that do not account for the inhomogeneity results in no loss of generality.

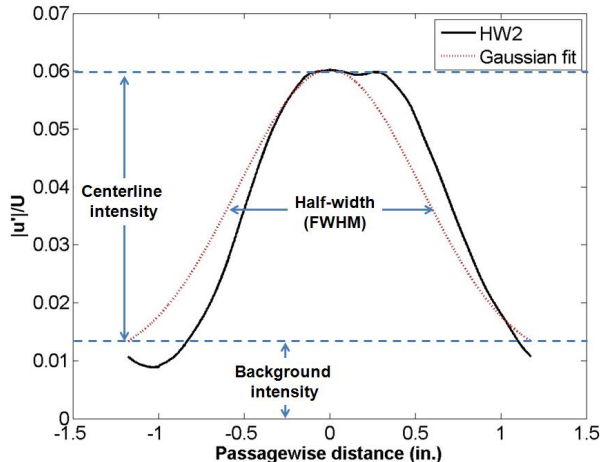


Figure 5. Gaussian representation of turbulence intensity.

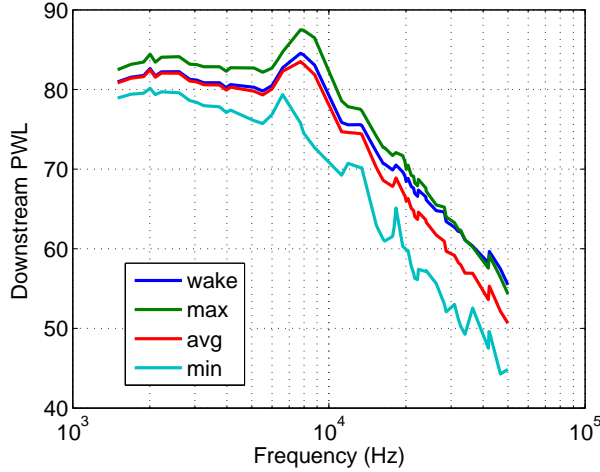


Figure 6. Effect of including TKE inhomogeneity across the passage. SDT baseline vanes at approach. Leading edge stagger. Liepmann spectral model.

E. Effect of varying the form of the turbulence correlation function on the final prediction.

The form of the correlation function that is selected greatly impacts the final results. As such, effort has been made to deduce which form is best suited to this application.

The correlation functions that generate the regularly used 3D turbulence spectra are described in Section II.B. The modeled longitudinal and lateral turbulence velocity correlations can be compared to the actual functions. Figure 7 shows the longitudinal and lateral correlation functions derived from the experimental hot-wire data for the approach SDT case (at the position just upstream of the leading edge of the vane) near midspan. The autocorrelation based length scale in the longitudinal and lateral directions were computed

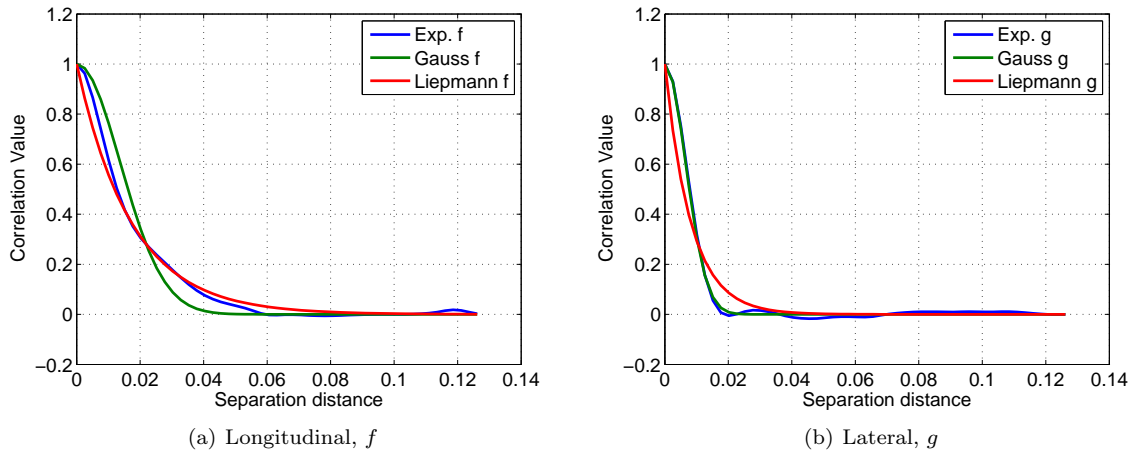


Figure 7. Longitudinal and lateral correlation functions, f and g . Curve fits of the experimental data based on Liepmann and Gaussian generating functions.

from the experimental data also. These quantities were used in the Liepmann and Gaussian models given in Eqs. (23) and the results are also shown in Figure 7. It is seen that the Liepmann form with the longitudinal length scale better fits the experimental longitudinal correlation. However, the Gaussian model with the

length scale of the lateral correlation better fits the experimental lateral correlation.

To further investigate the isotropic assumption behind the spectra defined in Section II.B, the connection between the longitudinal and lateral correlation functions can be considered.

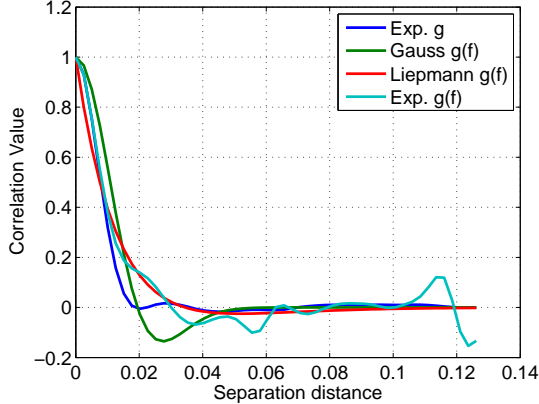


Figure 8. Comparison of various methods to define the lateral correlation function. Normalized by the lateral turbulence intensity.

makes the model possible, a decision must be made as to which generating function best fits the data. The author’s opinion is that the Liepmann model seems to do the best job overall, when focusing on the midspan region. In the future this will be considered more in depth and more attention will be given to other spanwise locations.

In addition to how the isotropic assumption and the choice of generating function affect the ability to model the inflow turbulence spectrum, its overall effect on the prediction of the broadband noise is also of interest. Figure 9 shows the predicted broadband noise when the Liepmann and Gaussian models are used as well as the nontraditional spectrum function derived with the RSI formulation (see Eq. (53)). It is noted that the results in the figure are all generated using only the 0th spanwise wavenumber. The RSI spectrum gives the best agreement with the experimental data. The large discrepancy between the results from the RSI spectrum function (Eq.(53)) and the usual 3D spectrum (Eq. (23) and (13)) without k_3 can be understood by simply

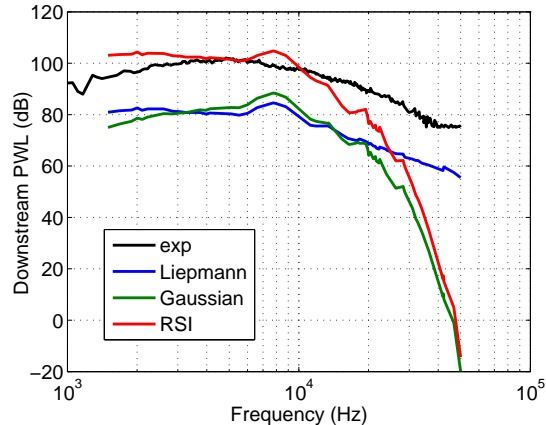


Figure 9. Comparison of broadband noise prediction using 3 different turbulence spectra: Liepmann, Gaussian, original RSI. SDT baseline vane case at approach. Leading edge stagger.

studying there forms.

$$\Phi_{Gaussian} = u_1^2 \frac{\Lambda_L^2}{\pi^4} (k_1 \Lambda_L)^2 \Lambda_L e^{-(k_1 \Lambda_L)^2 / \pi} e^{-(k_2 \Lambda_L)^2 / \pi} \quad (24)$$

$$\Phi_{RSI} = 8u_1^2 \Lambda_L \Lambda_T \Lambda_T e^{-(k_1 \Lambda_L)^2 / \pi} e^{-(k_2 \Lambda_T)^2 / \pi} \quad (25)$$

Here an additional $2\Lambda_T$ has been included in the RSI spectrum which does not actually appear in the RSI formulation until the one dimensional correlation function $R_r(r)$ is integrated. If the relationship between the length scales is taken as $\Lambda_T = \Lambda_L/2$, then the ratio of the two spectra is

$$\frac{\Phi_{Gaussian}}{\Phi_{RSI}} = \frac{(k_1 \Lambda_L)^2}{2\pi^4} e^{-(k_1 \Lambda_L/2)^2 / \pi} \quad (26)$$

which can be quite a small number for nominal values of k_1 and Λ_1 . This difference in the Φ values easily accounts for the - 20 dB difference seen in Figure 9.

F. Effect of the 2D flat-plate, strip-theory vane model as compared to the 3D cambered vane model.

In this section, RSI results are compared with results from BB3D. The two methods have been described briefly in Section II. The low count vane geometry at the approach condition is used for all of the comparisons in this section. A comparison between the vane unsteady pressure distribution is shown first. Preliminary validation showed that the core cascade aerodynamic solver used by RSI produces an unsteady pressure distribution equivalent to the results from LINC (a 2D flat plate cascade response code) which has been used by Logue for 2D-3D comparisons in the past.¹⁵ Figure 10 shows the comparison for a case that matches the flow and geometry of the low count vane at approach SDT case. The midspan information is used for the 2D simulation. The frequency is 5000 Hz, mode number is $m_g = 20$, the total Mach number is 0.4093, stagger angle is 17.5° , reduced frequency based on half chord is $k_1 = 9.128$, spacing is 0.6265, and interblade phase angle is 4.833. The 2D comparison is exact. The figure also shows the midspan pressure distribution

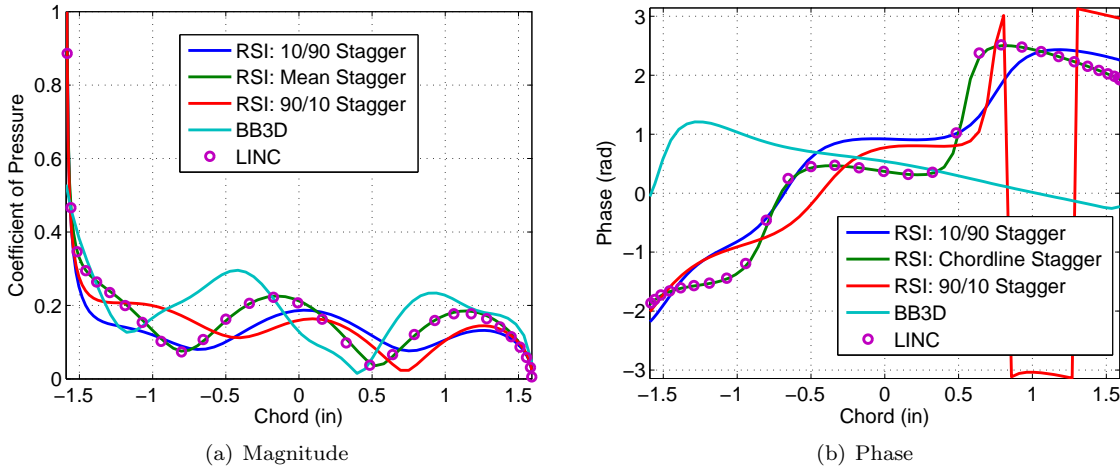


Figure 10. 2D-3D comparison. ΔC_p from leading edge to trailing edge. Low count vane, midspan, mean stagger, approach. $f = 5kHz$, $m_g = 20$.

obtained via the 3D simulation for the low count vane, approach case. The 3D result at midspan is quite different.

Because the selection of the stagger angle for the flat-plate vane impacts the prediction strongly, both the leading edge stagger and trailing edge stagger angles were tested as well as the mean stagger of the 3D

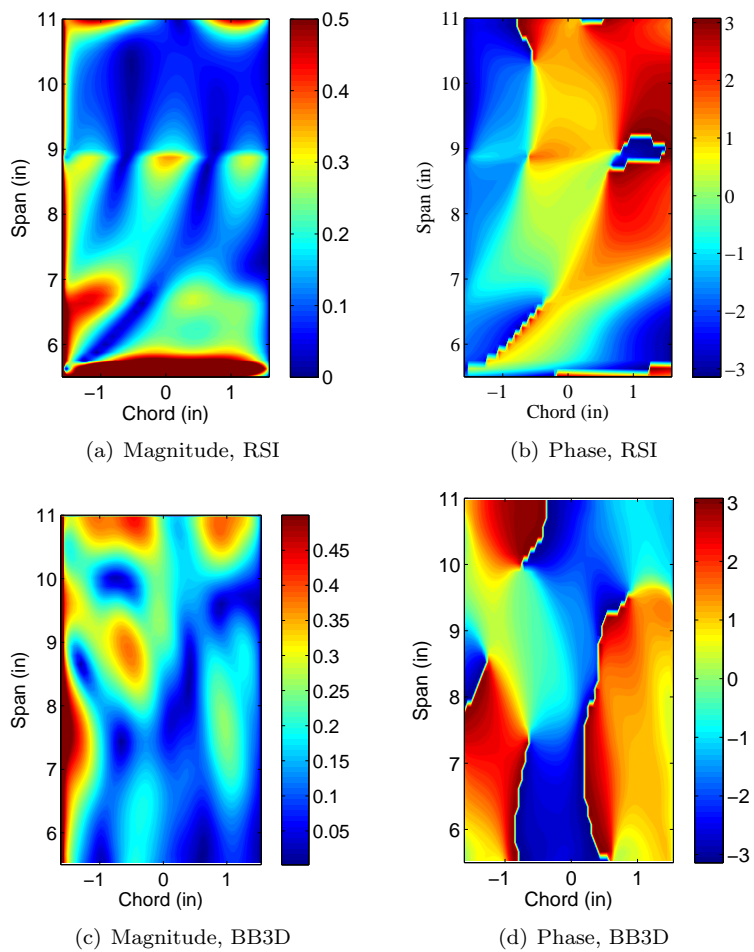


Figure 11. 2D-3D comparison. Magnitude and phase of ΔC_p on the vane. Low count vane, midspan, mean stagger, approach. $f = 5kHz$, $m_g = 20$.

vane model. The results are all presented in Figure 10. None of the stagger choices show better agreement with the 3D result.

The full predicted vane loading from hub-to-tip for the low-count vane at approach is shown two ways. First, Figure 11 compares the 2D and 3D predictions of the magnitude of the unsteady pressure jump. The cascade resonances that occur in the 2D strip simulation are apparent in the figure. Second, Figure 12 compares the lift distribution. Again the resonance can be seen. The radial phase distribution of the lift compares remarkably well from 2D to 3D, but the magnitude is completely different. Stagger angle selection does not improve the comparison. From previous investigations, it is noted that most likely the inclusion of actual finite extent accounts for the difference between 2D and 3D more so than the inclusion of camber.

The lift distribution for a lower frequency case was also considered. Figure 13 shows the results for the case of $f = 2500Hz$ and $m_g = 20$. The comparison is no worse or better at this frequency.

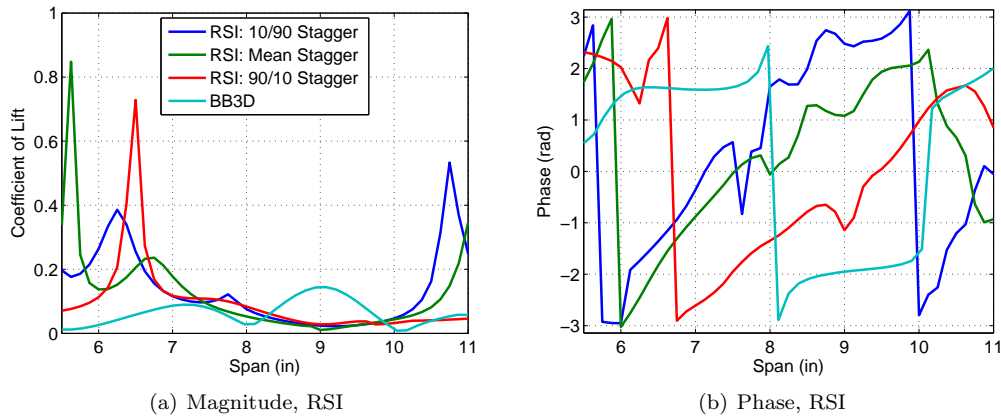


Figure 12. 2D-3D comparison. c_l distribution on the vane. Low count vane, RSI: mean stagger, approach. $f = 5kHz$, $m_g = 20$.

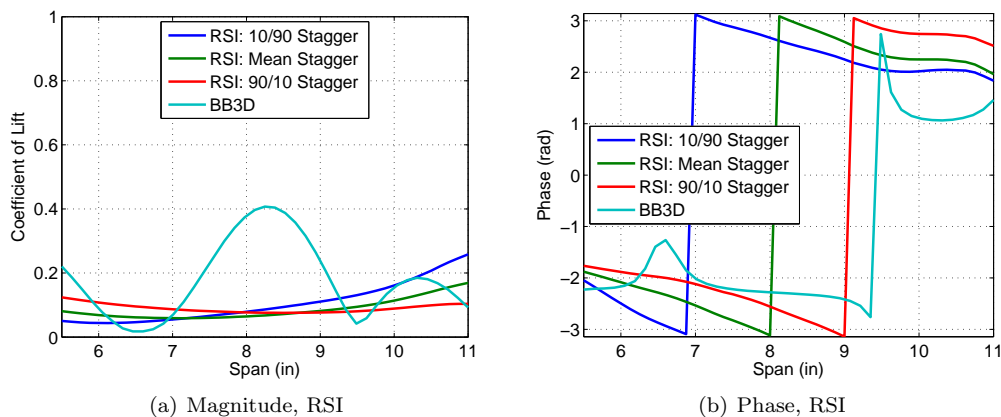


Figure 13. 2D-3D comparison. c_l distribution on the vane. Low count vane, RSI: mean stagger, approach. $f = 2.5kHz$, $m_g = 20$.

Another interesting feature that changes when one goes from 2D strip theory to 3D is the effect of mode number. For the 2D flat-plate cascade, one must only compute the response to gusts with mode numbers $0 - NV$ where NV is the number of vanes. All other modes, be they negative or higher positive modes, can be referenced to one of the basic modes. This is due to the periodicity that occurs in the interblade phase

angle and that the fact that the transverse gust is assumed to be in phase from strip to strip. However, for 3D simulations this periodicity and phase relation no longer exists.

As an example, the unsteady lift distribution on the flat-plate approximation to the low count vane geometry (26 vanes) for the case of $f = 5kHz$, $m_g = 14$ is exactly the same as that for the case of $f = 5kHz$ and $m_g = 40$. However, the unsteady lift response for the 3D cambered vane for these two cases is very different. The results are also shown in Figure 14. The 3D results are intriguing because they show a connection between the mode number and radial influence that is remarkably similar to a k_3 effect. Physically this follows because the wake alignment along the span introduces a phase lag (which would change substantially as the mode number changes) which is not modeled in the 2D strip approach. One would think this effect is more important for tonal noise where the wake position is of great interest. How this should affect the turbulent problem is a bit unclear.

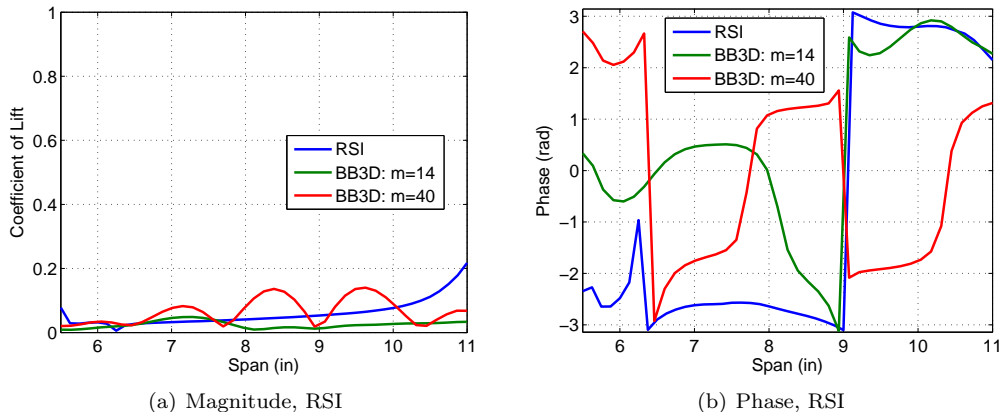


Figure 14. 2D-3D comparison. Mode number effect. c_l distribution on the vane. Low count vane, RSI: mean stagger, approach. $f = 5kHz$, $m_g = 14, 40$.

The clear differences in the unsteady surface pressure distribution when using 2D and 3D will ultimately lead to different predictions of the duct acoustics. Previously the BB3D code was used to simulate the low count vane at approach and good agreement with the experimental data was shown. The three-dimensional Lipemann spectrum was utilized. Those results together with results from the RSI method are given in Figure 16. RSI was run using three different spectra a) RSI, b) Liepmann - $k_3 = 0$, c) Gauss - $k_3 = 0$. Just as for the baseline vane case, the RSI spectrum gives the best agreement with the experimental data and the Liepmann and Gaussian spectra lead to 20 dB lower predictions. When the k_3 effect is added to the RSI calculations with the Liepmann spectrum now taken in the full three-dimensional sense, the results increase by about 10 dB. However, they still do not agree as well as with experiment as the results do from BB3D and RSI with the nontraditional spectrum.

It is noted that the input data for the BB3D simulation were derived from CFD analysis and the average passage value of the TKE was used to determine the turbulence intensity at each radial location. These input data were used for the RSI simulations shown in Figure 16. The difference between the computationally based input and the experimentally based input used for comparison of the unsteady vane loading shown earlier in this section can be seen in in Figure 15. The differences would not produce great variation in the vane responses above. So those results are still relevant as the foundation for the field acoustics.

It is noted that the 2D strip theory vane response together with the RSI spectrum compares well with the 3D vane response together with the Liepmann spectrum. However, the 2D strip theory vane response together with the Liepmann does not compare well. There is little that can be pulled from the physics behind these models to explain this phenomenon at this time. In the future a fourth combination, 3D vane response together with RSI spectrum, will be considered. This will be done by modeling a 3D uncambered vane and utilizing the Green's function method with the RSI spectrum to obtain the exhaust noise levels.

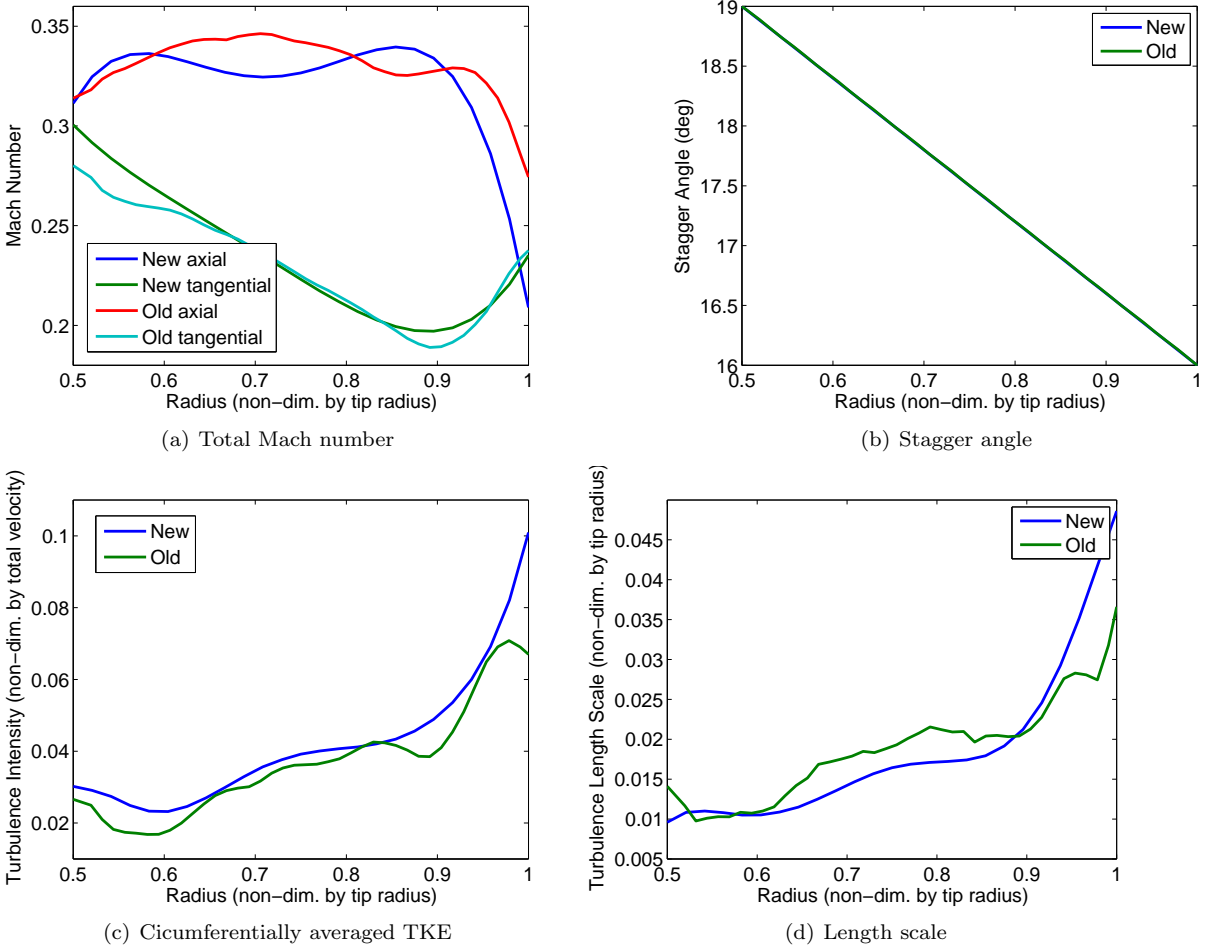


Figure 15. Input data at approach based on experiment and CFD.

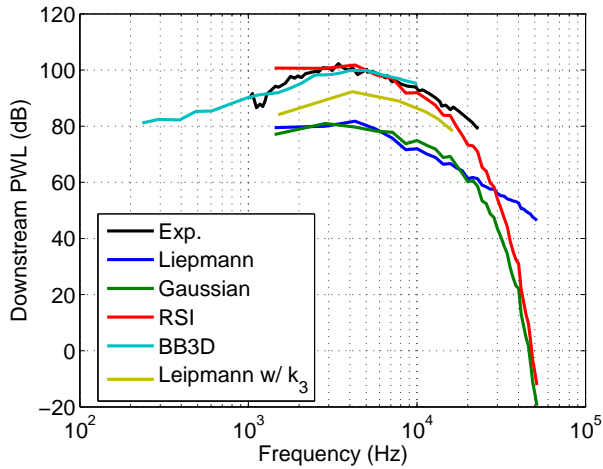


Figure 16. 2D-3D comparison. Exhaust PWL. Low count vane, RSI: mean stagger, approach. Liepmann and Gaussian.

V. Conclusions and Future Work

The focus of this paper is assessment of modeling choices available for broadband turbofan, fan-stage, interaction noise. The impact of six different modeling choices were considered. Two solid outcomes arise from the six investigations. First, the Green’s function method can be utilized as long as the frequencies are selected *a priori* to ensure that no frequencies correspond to singular duct modes. Second, there is little gained by including the inhomogeneity of the turbulence intensity in the passage. This means that a simpler formulation can be obtained following the RSI approach and that the input parameters are more easily derived from experiment or computation because average passage values of the turbulence intensity can be utilized.

A simple update to the previously presented RSI formulation for the correlation function to ensure that it leads to the correct integral length scale definition and to remove an imposed periodicity condition in the azimuthal direction is given. The largest impact of these changes comes from the exclusion of the periodicity condition as it significantly increases the high frequency roll-off. A ruling is still needed as to whether the periodicity condition is physically supported.

The impacts of the other effects are not easily separated. These include the model of the turbulence velocity spectrum and the use of 2D strip theory vs. 3D vane response models. It is clear that the 3D method does not give rise to cascade resonances along the span of the vane like the 2D method does. It is also clear that the behavior of the vane response with mode number is different in the 2D and 3D methods. However, it is not clear yet how these differences specifically impact the predicted exhaust noise.

Further comparison between the 2D and 3D models is needed to illuminate exactly which features are important to include. For instance, it is planned that a three-dimensional flat vane be simulated in BB3D. In addition, differences between the vane response will highlight whether the 3D nature of the vane or the cambered nature of the vane is the most important aspect. Previous results indicate that the inclusion of camber is not so important for the vane response.¹⁵ However, the inclusion of camber eliminates the need to guess at a stagger angle.

Further investigation of the longitudinal and lateral correlation functions, f and g , is planned. It is also surmised that a method for incorporating the experimental data into the definition of the spectrum will help sort out some of the spectral modeling issues. The inclusion of k_3 on the strips is still unsettling. More careful investigation as to which spanwise wave numbers actually contribute to the final solution is necessary in order to ensure compatibility between the inclusion of this effect, the selection of strip size, and the correlation length scale.

Acknowledgments

The authors would like to thank Dr. Envia for his continued support and sharing of the RSI code and Professor Hafiz Atassi for access to BB3D. Finally the authors acknowledge the financial support of the Aeroacoustics Research Consortium through the Ohio Aerospace Institute grant R-700-400301-40125 and the collaboration of the AARC members.

References

- ¹Atassi, H. and Vinogradov, I. V., “A model for fan broadband interaction noise in nonuniform flow,” *AIAA Paper No. 2005-2880*, 2005, 11th AIAA/CEAS Aeroacoustics Conference.
- ²Nallasamy, M. and Envia, E., “Computation of rotor wake turbulence noise,” *Journal of Sound and Vibration*, Vol. 282, 2005, pp. 649–678.
- ³Envia, E., Tweedt, D., Woodward, R. P., Elliot, D. M., Fite, E. B., Hughes, C. E., Podboy, G. G., and Sutliff, D. L., “Assessment of Current Fan Noise Prediction Capability,” *AIAA Paper No.2008-2991*, 2008, 14th AIAA/CEAS Aeroacoustics Conference.
- ⁴Maunus, J., Grace, S. M., and Sondak, D. L., “Effect of Rotor Wake Structure on Fan Interaction Noise,” *AIAA Paper No. AIAA 2010-3746*, 2010, 16th AIAA/CEAS Aeroacoustics Conference.
- ⁵Grace, S. M., Maunus, J. R., and Sondak, D. L., “Effect of CFD Wake Prediction in a Hybrid Simulation of Fan Broadband Interaction Noise,” *AIAA Paper No. AIAA 2011-2875*, 2011, 17th AIAA/CEAS Aeroacoustics Conference.

⁶Ventres, C., Theobald, M. A., and Mark, W. D., “Turbofan Noise Generation Volume 1: Analysis,” Tech. Rep. CR-167952, NASA, July 1982.

⁷Logue, M. M., *Sound Generation and Scattering in Turbofan Engines*, PhD Thesis, The University of Notre Dame, Notre Dame, IN, April 2010.

⁸Goldstein, M. E., *Aeroacoustics*, McGraw-Hill International Book Co., New York, etc., 1976.

⁹Grace, S. M., Sondak, D. L., Dorney, D. J., and Logue, M., “CFD Computation of Fan Interaction Noise,” *Proceedings of ASME IMECE*, Vol. IMECE2007-43779, Seattle, WA, 2007.

¹⁰Hinze, J. O., *Turbulence*, McGraw-Hill International Book Co., New York, etc., 1975.

¹¹Pope, S. B., *Turbulent Flows*, Cambridge University Press, Cambridge, UK, 2000.

¹²Atassi, H. M. and Logue, M. M., “Effect of Turbulence Structure on Broadband Fan Noise,” *AIAA Paper No. 2008-2842*, 2008, 14th AIAA/CEAS Aeroacoustics Conference.

¹³Podboy, G. G., Krupar, M. J., Helland, S. M., and Hughes, C., “Steady and Unsteady Flow Field Measurements Within a NASA 22-Inch Fan Model,” Tech. Rep. TM-2003-212329, NASA, 2003.

¹⁴Woodward, R. P., “Fan Noise Source Diagnostic Test-Farfield Acoustic Results,” *AIAA Paper No. 2002-2427*, 2002, 8th AIAA/CEAS Aeroacoustics Conference.

¹⁵Logue, M. M., Atassi, H. M., Topol, D. A., and Gilson, J. J., “Aerodynamics and Acoustics of a 3D Annular Cascade - Comparison with a 2D Linear Cascade,” *AIAA Paper No. 2010-3870*, 2010, 16th AIAA/CEAS Aeroacoustics Conference.

¹⁶Possou, H., Moreau, S., and Roger, M., “Broadband noise prediction of fan outlet guide vane using a cascade response function,” *Journal of Sound and Vibration*, Vol. 330, 2011, pp. 6153–6183.

¹⁷Morin, B. L., “Broadband Fan Noise Prediction System for Turbofan Engines,” Tech. Rep. NASA/CR-2010-216898, NASA, 2010.

VI. Appendix: RSI updates

A few changes have been made to the original RSI formulation. The impact of these changes on the predictions is shown in this section. First, the original formulation required that the correlation function be periodic with full revolution in the circumferential direction. This meant that the correlation function was rewritten as

$$R(\vec{X}, \Delta r) = \frac{1}{2\pi r} \sum_{s=-\infty}^{\infty} \phi(X_1, \frac{s}{r}, \Delta r) e^{isX_2/\bar{r}} \quad (27)$$

In the current version, from which the results in this paper are derived, this periodicity is not imposed.

Second, the original formulation utilized a form of the longitudinal correlation function that in physical space was given by

$$f_1(x, \Lambda_1) = e^{-\pi(x/\Lambda_1)^2} \quad (28)$$

This satisfies a nontraditional length scale relation

$$\int_{-\infty}^{\infty} f_1(x, \Lambda_1) dx = \Lambda_1 \quad (29)$$

however, it is more common to define the length scale as

$$\int_0^{\infty} f(x, \Lambda_1) dx = \Lambda_1 \quad (30)$$

Therefore, the correlation function should be given as

$$f(x, \Lambda_1) = e^{-\frac{\pi}{4}(x/\Lambda_1)^2} \quad (31)$$

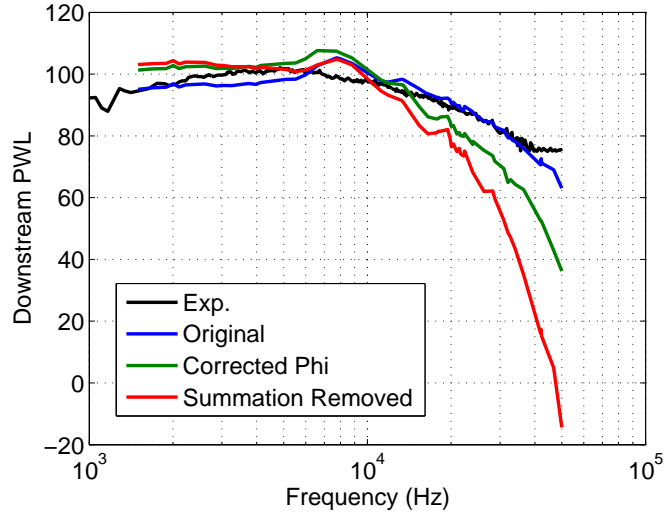


Figure 17. Affect of updating the correlation function. Baseline vane case at approach condition. RSI correlation function.

Figure 17 shows how these changes to the definition of the spectrum affect the final prediction. The prediction made with the original correlation function is shown for reference as well as the measured spectrum. Then

the green line shows the change that occurs when the correlation function is changed to satisfy the correct length scale requirement. This correction rotates the curve a bit about 12 kHz bringing the 1.4 kHz up about 8 dB and taking the 20 kHz down the same. The red curve uses the corrected correlation function and removes the periodicity condition from the correlation function. No change at the lower frequencies is seen but a drastic increase in the roll-off at the higher frequency occurs.

VII. Appendix: RSI Formulation

A. Upwash

Throughout this appendix, the arrow over a quantities denotes 2D vector (e.g. $\vec{X} = (X_1, X_2)$). Also, because just the upwash velocity is considered here the subscript notation normally used to describe turbulence is not used (e.g. $R = R_{22}$). The velocity fluctuations normal to the surface of the vanes can be assumed to have the following form.

$$w(\vec{X}, r, t) \approx w(\vec{X} - \vec{W}t, r) = F(\vec{X} \cdot \hat{n}, r)g(\vec{X} - \vec{W}t, r)$$

Where the ‘‘frozen gust’’ assumption is used to approximate the dependence on \vec{X} and t independently by the linked argument $\vec{X} - \vec{W}t$. Here the vectors \vec{X} , \vec{W} , and \hat{n} are taken to be in the moving rotor frame with \vec{W} being the mean flow velocity and \hat{n} being the unit normal to the stator vane. The correlation function of the upwash can be written as

$$\langle w(\vec{X} - \vec{W}t, r_1)w^*(\vec{Y} - \vec{W}\tau, r_2) \rangle = F(\vec{X} \cdot \hat{n}, r_1)F^*(\vec{Y} \cdot \hat{n}, r_2)\Phi(\vec{X} - \vec{Y} + \vec{W}(t - \tau), \Delta r), \quad (32)$$

where

$$R(\vec{X} - \vec{Y} - \vec{W}(t - \tau), \Delta r) = \langle g(\vec{X} - \vec{W}t, r_1)g^*(\vec{Y} - \vec{W}\tau, r_2) \rangle$$

and $\Delta r = r_1 - r_2$. The function F describes the variation of RMS turbulence normal to the vane and Φ is a correlation function relating to the length scale of the turbulence. Both will be formally defined later in the derivation.

The desired result is the Fourier transform of the upwash correlation function with respect to both time and space in the stationary stator frame. Using the transform pair

$$s(x, t) = \frac{1}{4\pi^2} \int_{-\infty}^{\infty} \int_{-\infty}^{\infty} \hat{s}(\lambda) e^{-i\omega t + i\lambda x} d\lambda d\omega$$

$$\hat{s}(\lambda, \omega) = \int_{-\infty}^{\infty} \int_{-\infty}^{\infty} s(x) e^{i\omega t - i\lambda x} dx dt,$$

where s is an arbitrary function and \hat{s} is its Fourier transform, we can write the desired result as follows.

$$\langle \tilde{w}\tilde{w}^* \rangle = \left\langle \tilde{w}(\vec{k}, \omega) \tilde{w}^*(\vec{K}, \nu) \right\rangle = \iiint \iiint \langle w(\vec{x}, r_1, t) w^*(\vec{y}, r_2, \tau) \rangle e^{i\omega t - i\vec{k}\cdot\vec{x}} e^{-i\nu\tau + i\vec{K}\cdot\vec{y}} d\vec{x} d\vec{y} dt d\tau \quad (33)$$

Here the integrals all range from $-\infty$ to ∞ ; ω and ν are radial frequencies; and, \vec{k} and \vec{K} are wavenumbers. The $\tilde{\cdot}$ indicates transform in two spatial dimensions and time.

Since the upwash velocity is most easily defined in the rotor frame (as above), rather than carry out the integration in the stator frame, we will use the following transformation to move all quantities to the rotor frame.

$$\vec{X} = \vec{x} + \vec{D} + \Omega r_1 t \hat{e}_2$$

$$\vec{Y} = \vec{y} + \vec{D} + \Omega r_2 \tau \hat{e}_2 \quad (34)$$

Thus, we can rewrite (33) as follows.

$$\langle \tilde{w}\tilde{w}^* \rangle = \iiint \iiint \langle w(\vec{X} - \vec{W}t, r_1) w^*(\vec{Y} - \vec{W}\tau, r_2) \rangle \otimes e^{i\omega t - i\vec{k}\cdot(\vec{X} - \vec{D} - \Omega r_1 t \hat{e}_2)} e^{-i\nu\tau + i\vec{K}\cdot(\vec{Y} - \vec{D} - \Omega r_2 \tau \hat{e}_2)} d\vec{X} d\vec{Y} dt d\tau \quad (35)$$

Next, substituting in (32) and using

$$\begin{aligned} & \left. \begin{aligned} \vec{\xi} &= \vec{X} - \vec{Y} + \vec{W}(t - \tau) \\ \Rightarrow \vec{X} &= \xi + \vec{y} + \vec{W}(t - \tau) \end{aligned} \right\} \begin{array}{l} \text{Argument of } R \\ \vec{X} \text{ in terms of } \vec{\xi} \text{ and } \vec{Y} \end{array} , \end{aligned}$$

(35) can now be written in terms of $\vec{\xi}$ and \vec{Y} .

$$\begin{aligned} \langle \tilde{w}\tilde{w}^* \rangle &= \iiint\limits_V F((\vec{\xi} + \vec{Y}) \cdot \hat{n}, r_1) F^*(\vec{Y} \cdot \hat{n}, r_2) R(\vec{\xi}, \Delta r) \otimes \\ & e^{i\omega t - i\vec{k} \cdot ((\vec{\xi} + \vec{Y} + \vec{W}(t - \tau)) - \vec{D} - \Omega r_1 t \hat{e}_2)} e^{-i\nu\tau + i\vec{K} \cdot (\vec{Y} - \vec{D} - \Omega r_2 \tau \hat{e}_2)} d\vec{\xi} d\vec{Y} dt d\tau \end{aligned} \quad (36)$$

The integrations with respect to t and τ are performed, resulting in

$$\begin{aligned} \langle \tilde{w}\tilde{w}^* \rangle &= (2\pi)^2 \delta(\omega - \vec{k} \cdot \vec{W} + k_2 \Omega r_1) \delta(\nu - \vec{K} \cdot \vec{W} + K_2 \Omega r_2) \otimes \\ & \iint F((\vec{\xi} + \vec{Y}) \cdot \hat{n}, r_1) F^*(\vec{Y} \cdot \hat{n}, r_2) R(\vec{\xi}, \Delta r) \otimes \\ & e^{-i\vec{k} \cdot \vec{\xi}} e^{-i\vec{Y} \cdot (\vec{k} - \vec{K})} e^{i\vec{D} \cdot (\vec{k} - \vec{K})} d\vec{\xi} d\vec{Y} . \end{aligned} \quad (37)$$

The function F which describes the turbulence distribution across a passage can be modeled as a Gaussian distribution on top of background turbulence. This can be written as

$$u'(y) = u'_b + u'_w e^{-\pi \left(\frac{y}{\gamma}\right)^2}$$

where u' is the turbulence intensity at a position normal to the wake $y = \vec{X} \cdot \hat{n}$, u'_b is the background turbulence level, u'_w is the Gaussian height, and γ is a measure of the Gaussian width. F is periodic around the wheel and can thus be written as

$$F(y) = u'_b + u'_w \sum_{m=-\infty}^{\infty} e^{-\frac{\pi}{\gamma^2} (y + mh \cos \theta)^2} .$$

where $h = 2\pi r/B$. Then, using Poisson's Summation Formula,

$$\sum_n s(t + n\tau) = \frac{1}{\tau} \sum_{\alpha} \hat{s}\left(\frac{2\pi\alpha}{\tau}\right) e^{i2\pi\left(\frac{\alpha}{\tau}\right)t} ,$$

where s is a periodic function with period τ and \hat{s} is its Fourier transform, we can rewrite F as

$$F(y) = u'_b + \frac{u'_w \gamma}{h \cos \theta} \sum_{\alpha=-\infty}^{\infty} e^{-\frac{1}{4\pi} \left(\frac{2\pi\alpha\gamma}{h \cos \theta}\right)^2} e^{i2\pi\left(\frac{\alpha}{h \cos \theta}\right)y} .$$

Here θ is the stagger angle. When a width measurement is defined in the circumferential direction as $Lw = \gamma/\cos \theta$ (this is convenient because this corresponds to the width perpendicular to the duct axis as opposed to the wake) the final expression for F becomes

$$F(y) = u'_b + \frac{u'_w BLw}{2\pi r} \sum_{\alpha=-\infty}^{\infty} e^{-\frac{1}{4\pi} \left(\frac{\alpha BLw}{r}\right)^2} e^{i\left(\frac{\alpha}{r \cos \theta}\right)y} = u'_b + \frac{u'_w BLw}{2\pi r} \sum_{\alpha=-\infty}^{\infty} \hat{f}\left(\frac{\alpha BLw}{r}\right) e^{i\left(\frac{\alpha}{r \cos \theta}\right)y} \quad (38)$$

Using this definition of F , the $F(\dots)F^*(\dots)$ term from (37) can now be expanded as follows.

$$F\left((\vec{\xi} + \vec{Y}) \cdot \hat{n}\right) F^*\left(\vec{Y} \cdot \hat{n}\right) = \mathcal{F}_{ww} + \mathcal{F}_{bw} + \mathcal{F}_{bb} \quad (39a)$$

where

$$\mathcal{F}_{ww} = \left(\frac{u'_w BL_w}{2\pi r} \right)^2 \sum_{s_1=-\infty}^{\infty} \sum_{s_2=-\infty}^{\infty} \hat{f} \left(\frac{s_1 BL_w}{r} \right) \hat{f} \left(\frac{s_2 BL_w}{r} \right) e^{\frac{is_1 B}{r \cos \chi} (\vec{\xi} + \vec{Y}) \cdot \hat{n}} e^{-\frac{is_2 B}{r \cos \chi} \vec{Y} \cdot \hat{n}} \quad (39b)$$

$$\mathcal{F}_{bw} = \frac{u'_w u'_b BL_w}{\pi r} \sum_{s_3=-\infty}^{\infty} \hat{f} \left(\frac{s_3 BL_w}{r} \right) \left[e^{\frac{is_3 B}{r \cos \chi} (\vec{\xi} + \vec{Y}) \cdot \hat{n}} + e^{-\frac{is_3 B}{r \cos \chi} \vec{Y} \cdot \hat{n}} \right] \quad (39c)$$

$$\mathcal{F}_{bb} = (u'_b)^2 \quad (39d)$$

Substituting (39) into (37) brings the following result.

$$\langle \tilde{w} \tilde{w}^* \rangle = (2\pi)^2 \delta \left(\omega - \vec{k} \cdot \vec{W} + k_2 \Omega r_1 \right) \delta \left(\nu - \vec{K} \cdot \vec{W} + K_2 \Omega r_2 \right) [\mathbf{w}_{ww} + \mathbf{w}_{bw} + \mathbf{w}_{bb}] \quad (40a)$$

where

$$\mathbf{w}_{ww} = \iint \left(\frac{u'_w BL_w}{2\pi r} \right)^2 \sum_{s_1=-\infty}^{\infty} \sum_{s_2=-\infty}^{\infty} \hat{f} \left(\frac{s_1 BL_w}{r} \right) \hat{f} \left(\frac{s_2 BL_w}{r} \right) e^{\frac{is_1 B}{r \cos \chi} (\vec{\xi} + \vec{Y}) \cdot \hat{n}} e^{-\frac{is_2 B}{r \cos \chi} \vec{Y} \cdot \hat{n}} \otimes \quad (40b)$$

$$R(\vec{\xi}, \Delta r) e^{-i\vec{k} \cdot \vec{\xi}} e^{-i\vec{Y} \cdot (\vec{k} - \vec{K})} e^{i\vec{D} \cdot (\vec{k} - \vec{K})} d\vec{\xi} d\vec{Y}$$

$$\mathbf{w}_{bw} = \iint \frac{u'_w u'_b BL_w}{\pi r} \sum_{s_3=-\infty}^{\infty} \hat{f} \left(\frac{s_3 BL_w}{r} \right) \left[e^{\frac{is_3 B}{r \cos \chi} (\vec{\xi} + \vec{Y}) \cdot \hat{n}} + e^{-\frac{is_3 B}{r \cos \chi} \vec{Y} \cdot \hat{n}} \right] \otimes \quad (40c)$$

$$R(\vec{\xi}, \Delta r) e^{-i\vec{k} \cdot \vec{\xi}} e^{-i\vec{Y} \cdot (\vec{k} - \vec{K})} e^{i\vec{D} \cdot (\vec{k} - \vec{K})} d\vec{\xi} d\vec{Y}$$

$$\mathbf{w}_{bb} = \iint (u'_b)^2 R(\vec{\xi}, \Delta r) e^{-i\vec{k} \cdot \vec{\xi}} e^{-i\vec{Y} \cdot (\vec{k} - \vec{K})} e^{i\vec{D} \cdot (\vec{k} - \vec{K})} d\vec{\xi} d\vec{Y} \quad (40d)$$

The integration with respect to \vec{Y} can now be performed on Equations (40b-40d).

$$\mathbf{w}_{ww} = (2\pi)^2 \left(\frac{u'_w BL_w}{2\pi r} \right)^2 \sum_{s_1=-\infty}^{\infty} \sum_{s_2=-\infty}^{\infty} \hat{f} \left(\frac{s_1 BL_w}{r} \right) \hat{f} \left(\frac{s_2 BL_w}{r} \right) e^{i\vec{D} \cdot (\vec{k} - \vec{K})} \otimes$$

$$\delta \left(-(\vec{k} - \vec{K}) + \frac{(s_1 - s_2) B}{r \cos \chi} \hat{n} \right) \int R(\vec{\xi}, \Delta r) e^{i\vec{\xi} \cdot \left(\frac{s_1 B}{r \cos \chi} \hat{n} - \vec{k} \right)} d\vec{\xi}$$

$$\mathbf{w}_{bw} = (2\pi)^2 \frac{u'_w u'_b BL_w}{\pi r} \sum_{s_3=-\infty}^{\infty} \hat{f} \left(\frac{s_3 BL_w}{r} \right) e^{i\vec{D} \cdot (\vec{k} - \vec{K})} \int R(\vec{\xi}, \Delta r) e^{-i\vec{k} \cdot \vec{\xi}} \otimes$$

$$\left[e^{\frac{is_3 B}{r \cos \chi} \vec{\xi} \cdot \hat{n}} \delta \left(-(\vec{k} - \vec{K}) + \frac{s_3 B}{r \cos \chi} \hat{n} \right) + \delta \left(-(\vec{k} - \vec{K}) - \frac{s_3 B}{r \cos \chi} \hat{n} \right) \right] d\vec{\xi}$$

$$\mathbf{w}_{bb} = (2\pi)^2 (u'_b)^2 \delta \left(-(\vec{k} - \vec{K}) \right) e^{i\vec{D} \cdot (\vec{k} - \vec{K})} \int R(\vec{\xi}, \Delta r) e^{-i\vec{k} \cdot \vec{\xi}} d\vec{\xi}$$

Now, note that in each case, the remaining integration is simply the Fourier transform of the function R . Therefore, we can write

$$\mathbf{w}_{ww} = (2\pi)^2 \left(\frac{u'_w BL_w}{2\pi r} \right)^2 \sum_{s_1=-\infty}^{\infty} \sum_{s_2=-\infty}^{\infty} \hat{f} \left(\frac{s_1 BL_w}{r} \right) \hat{f} \left(\frac{s_2 BL_w}{r} \right) e^{i\vec{D} \cdot (\vec{k} - \vec{K})} \otimes$$

$$\delta \left(\vec{K} - \vec{k} + \frac{(s_1 - s_2) B}{r \cos \chi} \hat{n} \right) \Phi \left(\vec{k} - \frac{s_1 B}{r \cos \chi} \hat{n}, \Delta r \right) ,$$

$$\mathbf{w}_{bw} = (2\pi)^2 \frac{u'_w u'_b BL_w}{\pi r} \sum_{s_3=-\infty}^{\infty} \hat{f} \left(\frac{s_3 BL_w}{r} \right) e^{i\vec{D} \cdot (\vec{k} - \vec{K})} \left[\Phi \left(\frac{\vec{k} - is_3 B}{r \cos \chi} \hat{n}, \Delta r \right) \otimes$$

$$\delta \left(\vec{K} - \vec{k} + \frac{s_3 B}{r \cos \chi} \hat{n} \right) + \Phi \left(\vec{k}, \Delta r \right) \delta \left(\vec{K} - \vec{k} - \frac{s_3 B}{r \cos \chi} \hat{n} \right) \right] ,$$

and

$$\mathfrak{w}_{bb} = (2\pi)^2 (u'_b)^2 \delta(\vec{K} - \vec{k}) e^{i\vec{D} \cdot (\vec{k} - \vec{K})} \Phi(\vec{k}, \Delta r) \quad .$$

Looking back at (40a), we can now rewrite the arguments to its two delta functions. First, note that the term $-\vec{k} \cdot \vec{W} + k_2 \Omega r_1$ from the first delta function in (40a) can be simplified as follows.

$$-\vec{k} \cdot \vec{W} + k_2 \Omega r_1 = \vec{k} \cdot (-\vec{W} + \Omega r \hat{e}_2) = -\vec{k} \cdot \vec{U}_r$$

Thus, the first delta function from (40a) can be written as $\delta(\omega - \vec{k} \cdot \vec{U}_r)$. Next, using the delta functions generated in $\mathfrak{w}_{ww, bw, bb}$ when the integration with respect to \vec{Y} was performed, the second delta function can be rewritten for each of the \mathfrak{w} 's, respectively.

$$\begin{aligned} \mathfrak{w}_{ww} : \quad & 1) \quad \left\{ \delta \left(\vec{K} - \vec{k} + \frac{(s_1 - s_2) B}{r \cos \chi} \hat{n} \right) \Rightarrow K_2 = k_2 + \frac{(s_2 - s_1) B}{r} \right. \\ & 2) \quad \left\{ \begin{aligned} -\nu + \vec{k} \cdot \vec{W} - K_2 \Omega r &= -\nu + \vec{k} \cdot \vec{W} - \left(k_2 + \frac{(s_2 - s_1) B}{r} \right) \Omega r \\ &= -\nu + \vec{k} \cdot \vec{U}_r - \Omega (s_2 - s_1) r \end{aligned} \right. \\ & 3) \quad \left\{ \delta \left(\omega - \vec{k} \cdot \vec{U}_r \right) \Rightarrow \omega = \vec{k} \cdot \vec{U}_r \right. \\ & \Rightarrow \delta \left(-\nu + \vec{k} \cdot \vec{W} - K_2 \Omega r \right) = \delta \left(\nu - \omega + \Omega (s_2 - s_1) B \right) \\ \mathfrak{w}_{bw} : \quad & 1a) \quad \left\{ \delta \left(\vec{K} - \vec{k} + \frac{s_3 B}{r \cos \chi} \hat{n} \right) \Rightarrow K_2 = k_2 + \frac{s_3 B}{r} \right. \\ & 2a) \quad \left\{ \begin{aligned} -\nu + \vec{k} \cdot \vec{W} - K_2 \Omega r &= -\nu + \vec{k} \cdot \vec{W} - \left(k_2 + \frac{s_3 B}{r} \right) \Omega r \\ &= -\nu + \vec{k} \cdot \vec{U}_r - \Omega s_3 r \end{aligned} \right. \\ & 3a) \quad \left\{ \delta \left(\omega - \vec{k} \cdot \vec{U}_r \right) \Rightarrow \omega = \vec{k} \cdot \vec{U}_r \right. \\ & \Rightarrow \delta \left(-\nu + \vec{k} \cdot \vec{W} - K_2 \Omega r \right) = \delta \left(\nu - \omega + \Omega s_3 B \right) \\ & 1b) \quad \left\{ \delta \left(\vec{K} - \vec{k} - \frac{s_3 B}{r \cos \chi} \hat{n} \right) \Rightarrow K_2 = k_2 - \frac{s_3 B}{r} \right. \\ & 2b) \quad \left\{ \begin{aligned} -\nu + \vec{k} \cdot \vec{W} - K_2 \Omega r &= -\nu + \vec{k} \cdot \vec{W} - \left(k_2 - \frac{s_3 B}{r} \right) \Omega r \\ &= -\nu + \vec{k} \cdot \vec{U}_r + \Omega s_3 r \end{aligned} \right. \\ & 3b) \quad \left\{ \delta \left(\omega - \vec{k} \cdot \vec{U}_r \right) \Rightarrow \omega = \vec{k} \cdot \vec{U}_r \right. \\ & \Rightarrow \delta \left(-\nu + \vec{k} \cdot \vec{W} - K_2 \Omega r \right) = \delta \left(\nu - \omega - \Omega s_3 B \right) \\ \mathfrak{w}_{bb} : \quad & 1) \quad \left\{ \delta \left(\vec{K} - \vec{k} \right) \Rightarrow K_2 = k_2 \right. \\ & 2) \quad \left\{ \begin{aligned} -\nu + \vec{k} \cdot \vec{W} - K_2 \Omega r &= -\nu + \vec{k} \cdot \vec{W} - k_2 \Omega r \\ &= -\nu + \vec{k} \cdot \vec{U}_r \end{aligned} \right. \\ & 3) \quad \left\{ \delta \left(\omega - \vec{k} \cdot \vec{U}_r \right) \Rightarrow \omega = \vec{k} \cdot \vec{U}_r \right. \\ & \Rightarrow \delta \left(-\nu + \vec{k} \cdot \vec{W} - K_2 \Omega r \right) = \delta \left(\nu - \omega \right) \end{aligned}$$

Using these forms of the first delta functions, the final correlation function of the upwash can be written.

$$\langle \tilde{w}\tilde{w}^* \rangle = \mathfrak{W}_{ww} + \mathfrak{W}_{bw} + \mathfrak{W}_{bb} \quad (41a)$$

where

$$\begin{aligned} \mathfrak{W}_{ww} = & \left(\frac{2\pi BL_w u'_w}{r} \right)^2 \sum_{s_1=-\infty}^{\infty} \sum_{s_2=-\infty}^{\infty} \delta(\omega - \vec{k} \cdot \vec{U}_r) \delta(\nu - \omega + \Omega(s_2 - s_1)B) \otimes \\ & \hat{f}\left(\frac{s_1 BL_w}{r}\right) \hat{f}\left(\frac{s_2 BL_w}{r}\right) \delta\left(\vec{K} - \vec{k} + \frac{(s_1 - s_2)B}{r \cos \chi} \hat{n}\right) \otimes \\ & \Phi\left(\vec{k} - \frac{s_1 B}{r \cos \chi} \hat{n}, \Delta r\right) e^{i\vec{D} \cdot (\vec{k} - \vec{K})} \end{aligned} \quad (41b)$$

$$\begin{aligned} \mathfrak{W}_{bw} = & \frac{(2\pi)^3 BL_w u'_w u'_b}{r} \sum_{s_3=-\infty}^{\infty} \delta(\omega - \vec{k} \cdot \vec{U}_r) \delta(\nu - \omega - \Omega s_3 B) \hat{f}\left(\frac{s_3 BL_w}{r}\right) \otimes \\ & \delta\left(\vec{K} - \vec{k} + \frac{s_3 B}{r \cos \chi} \hat{n}\right) \left[\Phi\left(\vec{k} - \frac{s_3 B}{r \cos \chi} \hat{n}, \Delta r\right) + \Phi\left(\vec{k}, \Delta r\right) \right] e^{i\vec{D} \cdot (\vec{k} - \vec{K})} \end{aligned} \quad (41c)$$

$$\mathfrak{W}_{bb} = (2\pi)^4 (u'_b)^2 \delta(\omega - \vec{k} \cdot \vec{U}_r) \delta(\nu - \omega) \delta(\vec{K} - \vec{k}) \Phi\left(\vec{k}, \Delta r\right) e^{i\vec{D} \cdot (\vec{k} - \vec{K})} \quad (41d)$$

B. Pressure Spectrum

The pressure spectrum in the duct is defined by the following equation.

$$\begin{aligned} \langle \tilde{p}_{mn}(\omega) \tilde{p}_{mn}^*(\nu) \rangle = & \frac{1}{4\Gamma^2 k_{mn}(\omega) k_{mn}(\nu)} \int_{r_H}^{r_T} \int_{r_H}^{r_T} \int_{-b}^b \int_{-b}^b R(r_1, \omega) R(r_2, \nu) e^{i\mu(r_1, \omega) z_1} e^{-i\mu(r_2, \nu) z_2} \otimes \\ & \left\{ \sum_{j=0}^{V-1} e^{i2\pi \frac{mj}{V}} \sum_{l=0}^{V-1} e^{-i2\pi \frac{ml}{V}} \langle \Delta \tilde{p}_j(r_1, z_1, \omega) \Delta \tilde{p}_l^*(r_2, z_2, \nu) \rangle \right\} dz_2 dz_1 dr_1 dr_2 \end{aligned} \quad (42)$$

where

$$\begin{aligned} \Gamma &= \pi (r_t^2 - r_h^2) \\ k_{mn}(\omega) &= \sqrt{\left(\frac{\omega}{c_o}\right)^2 - \beta^2 \kappa_{mn}^2} \\ \kappa_{mn} &= \text{roots of Bessel function equation from the Green's function equation} \\ R(r, \omega) &= \left[\frac{m}{r} \cos \chi - \gamma_{mn}(\omega) \sin \chi \right] \Psi_m(\kappa_{mn} r) \\ \Psi_m &= \text{duct mode from the Green's function equation} \\ \mu(r, \omega) &= \gamma_{mn}(\omega) \cos \chi + \frac{m}{r} \sin \chi \\ \gamma_{mn}(\omega) &= \frac{M\omega}{\beta^2 c_o} + \frac{k_{mn}(\omega)}{\beta^2} \text{sign}(z_2 - z_1) \end{aligned}$$

The unsteady stator loading, $\langle \Delta \tilde{p}_j(r_1, z_1, \omega) \Delta \tilde{p}_l^*(r_2, z_2, \nu) \rangle$ can be computed given the upwash correlation derived in Section A. This may be done via the following formula.

$$\begin{aligned} \langle \Delta \tilde{p}_j(r_1, z_1, \omega) \Delta \tilde{p}_l^*(r_2, z_2, \nu) \rangle = & \frac{(\rho_o U_r)^2}{(2\pi)^4} \int_{-\infty}^{\infty} \int_{-\infty}^{\infty} \mathfrak{F}\left(r_1, z_1, \vec{k}, \omega\right) \mathfrak{F}^*\left(r_2, z_2, \vec{K}, \nu\right) \otimes \\ & e^{i\vec{j}\vec{k} \cdot \vec{H}} e^{-i\vec{l}\vec{K} \cdot \vec{H}} \langle \tilde{w}\tilde{w}^* \rangle d^2 \vec{K} d^2 \vec{k} \end{aligned} \quad (43)$$

Here, \mathfrak{F} is the cascade response due to a unit upwash. More specifically, \mathfrak{F} is defined as the solution to the integral equation,

$$e^{i(\vec{k}\cdot\vec{c})z} = \int_{-b}^b K_c(z-y) \mathfrak{F}(r, z, \vec{k}, \omega) \frac{dy}{b} \quad ,$$

where K_c is the kernel function derived in Appendix B of Ventres.⁶

Substituting (43) into (42) results in the following expression.

$$\begin{aligned} \langle \tilde{p}_{mn}(\omega) \tilde{p}_{mn}^*(\nu) \rangle &= \frac{1}{4\Gamma^2 k_{mn}(\omega) k_{mn}(\nu)} \frac{(\rho_o U_r)^2}{(2\pi)^4} \iiint R(r_1, \omega) R(r_2, \nu) e^{i\mu(r_1, \omega)z_1} e^{-i\mu(r_2, \nu)z_2} \otimes \\ &\quad \left\{ \sum_{j=0}^{V-1} \sum_{l=0}^{V-1} \iint \mathfrak{F} \mathfrak{F}^* e^{i2\pi j(\frac{m}{V} + \vec{k}\cdot\vec{H})} e^{-i2\pi l(\frac{m}{V} + \vec{K}\cdot\vec{H})} \langle \tilde{w} \tilde{w}^* \rangle d^2 \vec{K} d^2 \vec{k} \right\} dz_2 dz_1 dr_1 dr_2 \end{aligned} \quad (44)$$

This can be simplified through use of the identity,

$$\sum_{\alpha=0}^{N-1} e^{i2\pi\alpha c} = \begin{cases} N & \text{if } c \in \mathbb{Z} \\ 0 & \text{otherwise} \end{cases}$$

on the summations over j and l . First note that $\vec{H} = 2\pi r \hat{e}_2 / V$ and then it can be seen that

$$\begin{aligned} \sum_{j=0}^{V-1} e^{i2\pi j(\frac{m}{V} + \vec{k}\cdot\vec{H})} &= \begin{cases} V & \text{if } m + k_2 r = c_1 V \text{ with } c_1 \in \mathbb{Z} \\ 0 & \text{otherwise} \end{cases} \quad , \\ \text{and } \sum_{l=0}^{V-1} e^{-i2\pi l(\frac{m}{V} + \vec{K}\cdot\vec{H})} &= \begin{cases} V & \text{if } m + K_2 r = c_2 V \text{ with } c_2 \in \mathbb{Z} \\ 0 & \text{otherwise} \end{cases} \quad . \end{aligned}$$

For both sums, we wish to force the first case to happen. This can be done by using properties of the delta

functions contained in $\langle \tilde{w}\tilde{w}^* \rangle$ as well as changing the summation indices within $\langle \tilde{w}\tilde{w}^* \rangle$.

$$\begin{aligned}
\mathfrak{W}_{ww} : & \left\{ \begin{array}{l} \delta \left(\vec{K} - \vec{k} + \frac{(s_1 - s_2)B}{r \cos \chi} \hat{n} \right) \Rightarrow K_2 = k_2 + \frac{(s_2 - s_1)B}{r} \\ \therefore m + K_2 r = m + k_2 r + (s_2 - s_1)B = c_2 V \\ \left. \begin{array}{l} m + k_2 r = c_1 V \\ m + k_2 r + (s_2 - s_1)B = c_2 V \end{array} \right\} \Rightarrow s_1 - s_2 = (c_1 - c_2) \frac{V}{B} \\ s_1, s_2 \in \mathbb{Z} \Rightarrow s_1 - s_2 \in \mathbb{Z} \Rightarrow (c_1 - c_2) \frac{V}{B} \in \mathbb{Z} \\ \therefore c_1 - c_2 = qB \text{ with } q \in \mathbb{Z} \\ \text{Change summation indices to } s_1, c_1, \text{ and } q; \text{ Let } s_2 = s_1 - qV \end{array} \right. \\
\mathfrak{W}_{bw} : & \left\{ \begin{array}{l} \delta \left(\vec{K} - \vec{k} - \frac{s_3 B}{r \cos \chi} \hat{n} \right) \Rightarrow K_2 = k_2 - \frac{s_3 B}{r} \\ \therefore m + K_2 r = m + k_2 r - s_3 B = c_2 V \\ \left. \begin{array}{l} m + k_2 r = c_1 V \\ m + k_2 r - s_3 B = c_2 V \end{array} \right\} \Rightarrow -s_3 = (c_1 - c_2) \frac{V}{B} \\ s_3 \in \mathbb{Z} \Rightarrow (c_1 - c_2) \frac{V}{B} \in \mathbb{Z} \\ \therefore c_1 - c_2 = qB \text{ with } q \in \mathbb{Z} \\ \text{Change summation indices to } c_1 \text{ and } q; \text{ Let } s_3 = -qV \end{array} \right. \\
\mathfrak{W}_{ww} : & \left\{ \begin{array}{l} \delta \left(\vec{K} - \vec{k} \right) \Rightarrow K_2 = k_2 \\ \therefore m + K_2 r = m + k_2 r = c_1 V \\ \text{Add summation over } c_1 \end{array} \right.
\end{aligned}$$

In all cases, k_2 must now be defined as $k_2 = \frac{m - c_1 V}{r}$

The next step, is to note that the summations over q represent fluctuating variations and that dropping this index results in the time averaged value of the pressure spectrum. Applying this and substituting (41) into (43) and the result into (42) gives

$$\begin{aligned}
\langle \tilde{p}_{mn}(\omega) \tilde{p}_{mn}^*(\nu) \rangle &= \frac{1}{4\Gamma^2 k_{mn}(\omega) k_{mn}(\nu)} \iiint R(r_1, \omega) R(r_2, \nu) e^{i\mu(r_1, \omega) z_1} e^{-i\mu(r_2, \nu) z_2} \otimes \\
& \left\{ \iint \mathfrak{F} \mathfrak{F}^* \sum_{c_1=-\infty}^{\infty} \left[\left(\sum_{s_1=-\infty}^{\infty} W_{ww} \right) + W_{bw} + W_{bb} \right] \delta \left(\vec{K} - \vec{k} \right) \otimes \right. \\
& \left. \delta \left(k_2 + \frac{m - c_1 V}{r} \right) \delta \left(\omega - \vec{k} \cdot \vec{U}_r \right) \delta \left(\omega - \nu \right) d^2 \vec{K} d^2 \vec{k} \right\} dz_2 dz_1 dr_1 dr_2 \quad , \quad (45)
\end{aligned}$$

where

$$\begin{aligned}
W_{ww} &= \left(\frac{\rho_o U_r B V L_w u'_w}{2\pi r} \right)^2 \left| \hat{f} \left(\frac{s_1 B L_w}{r} \right) \right|^2 \Phi \left(\vec{k} - \frac{s_1 B}{r \cos \chi} \hat{n}, \Delta r \right) \\
W_{bw} &= \left(\frac{(\rho_o U_r)^2 B L_w u'_w u'_b}{2\pi r} \right) 2 \Phi \left(\vec{k}, \Delta r \right) \\
W_{bb} &= (\rho_o U_r V u'_b)^2 \Phi \left(\vec{k}, \Delta r \right)
\end{aligned}$$

Now, due to the Delta functions, performing the integrations with respect to \vec{K} and \vec{k} will result in all instances of \vec{K} being replaced by \vec{k} where \vec{k} is now defined as follows.

$$\begin{aligned}\vec{k} : \quad k_1 &= \frac{\omega}{U_{r,1}} + \frac{U_{r,2}}{U_{r,1}} k_2 \\ k_2 &= \frac{c_1 V - m}{r}\end{aligned}\tag{46}$$

C. Final Result

$$\langle \tilde{p}_{mn}(\omega) \tilde{p}_{mn}^*(\nu) \rangle = \frac{1}{4\Gamma^2 k_{mn}(\omega) k_{mn}(\nu)} \int_{r_H}^{r_T} \int_{r_H}^{r_T} R(\bar{r}, \omega) R(\bar{r}, \nu) \{\mathcal{P}\} C_{mn}(\bar{r}, \omega) C_{mn}^*(\bar{r}, \nu) d(\Delta r) d\bar{r}\tag{47a}$$

where

$$C_{mn}(\bar{r}, \omega) = \int_{-b}^b \mathfrak{F}(r, z, \vec{k}, \omega) e^{i\mu(\bar{r}, \omega)z} dz\tag{47b}$$

and

$$\begin{aligned}\mathcal{P} = (\rho U_r V)^2 \delta(\nu - \omega) \left\{ \sum_{c_1=-\infty}^{\infty} \left[\sum_{s_1=-\infty}^{\infty} \left(\left(\frac{BL_w u'_w}{2\pi \bar{r}} \right)^2 \left| \hat{f} \left(\frac{s_1 BL_w}{r} \right) \right|^2 \Phi \left(\vec{k} - \frac{s_1 B}{r \cos \chi} \hat{n}, \Delta r \right) \right) \right] \oplus \right. \\ \left. \left(\frac{BL_w u'_w u'_b}{\pi r} + (u'_b)^2 \right) \Phi(\vec{k}, \Delta r) \right\}\end{aligned}\tag{47c}$$

Now, everywhere \vec{k} is defined as follows.

$$\vec{k} : \quad k_1 = \frac{\omega}{U_{r_1}} - \frac{U_{r_2}}{U_{r_1}} k_2 \quad \text{and} \quad k_2 = \frac{c_1 V - m}{r}$$

D. RSI Turbulence Correlation Function

The turbulence correlation function R in the original formulation had the form

$$R(\vec{\xi}, \Delta r) = R_1(\xi_1) R_2(\xi_2) R_r(\Delta r)\tag{48}$$

with transform

$$\Phi(\vec{k}, \Delta r) = \Phi_1(k_1) \Phi_2(k_2) R_r(\Delta r)\tag{49}$$

The now corrected RSI assumes

$$R_1 = e^{-\frac{\pi}{4} \left(\frac{\xi_1}{\Lambda_1} \right)^2}\tag{50}$$

$$R_2 = e^{-\frac{\pi}{4} \left(\frac{\xi_2}{\Lambda_2} \right)^2}\tag{51}$$

such that

$$\hat{R}_1 = 2\Lambda_1 e^{-(k_1 \Lambda_1)^2 / \pi}\tag{52}$$

$$\hat{R}_2 = 2\Lambda_2 e^{-(k_2 \Lambda_2)^2 / \pi}\tag{53}$$